

# Feasibility of a Near-Surface Wave-Powered Profiling Float for Extended Fully Submerged Autonomous Deployments

Russell Shomberg<sup>1</sup>

Michael Jakuba<sup>2</sup>

Dana Yoerger<sup>2</sup>

**Abstract**—We propose a float capable of harvesting wave energy while fully submerged. The proposed design could theoretically operate indefinitely without ever breaching the surface. We developed and validated design guidelines for the proposed float through a combination and tank testing simulation. These design insights could be employed to build an operational float.

<sup>1</sup> University of Rhode Island Narragansett RI USA

<sup>2</sup> Woods Hole Oceanographic Institution Woods Hole MA USA

## I. INTRODUCTION AND BACKGROUND

Autonomous floats play an important role throughout the ocean sciences [1], [2], [3]. To extend deployments beyond battery life limitations, floats employ environmental energy harvesting such as solar [2], wind [4], and wave [5] energy. To our knowledge, all currently existing autonomous floats harvesting environmental energy utilize some kind of surface expression. This study explores a possible design for a autonomous wave energy converter (WEC) float capable of harvesting near-surface wave energy without breaching the surface. Harvesting environmental energy without a surface expression would enable stealth missions as well as reducing the risk of theft or vandalism [6].

Recent developments in wave power show that, for the scale of a scientific floats, oscillating body style WECs have the highest efficiencies [7]. Many oscillating body WECs harvest energy from the bobbing motion caused by buoyancy in oscillating flow for a semi-submerged body [8]. However, that design requires an exposed surface expression to create variable buoyant force. Alternatively, two-body systems can employ a buoyant surface float to drive a power take-off (PTO) system far below in the relatively still water [5]. Drifting wave-energy harvesting robotic systems of this format have been shown to be capable of generating power [9], holding station [10], and traversing long distances [11].

Unlike a conventional two-body body WECs which rely on buoyancy, our design would operate without direct coupling to the surface motion and must instead harvest energy from the orbital velocity of the water in the wave field. A submerged WEC must also overcome the exponential loss of wave energy with depth [12], so the device must operate close enough to surface to harvest the required

energy. However, due to the unpredictable nature of ocean waves, the risk of a surface breach increases with proximity to the surface therefore requiring an active control system.

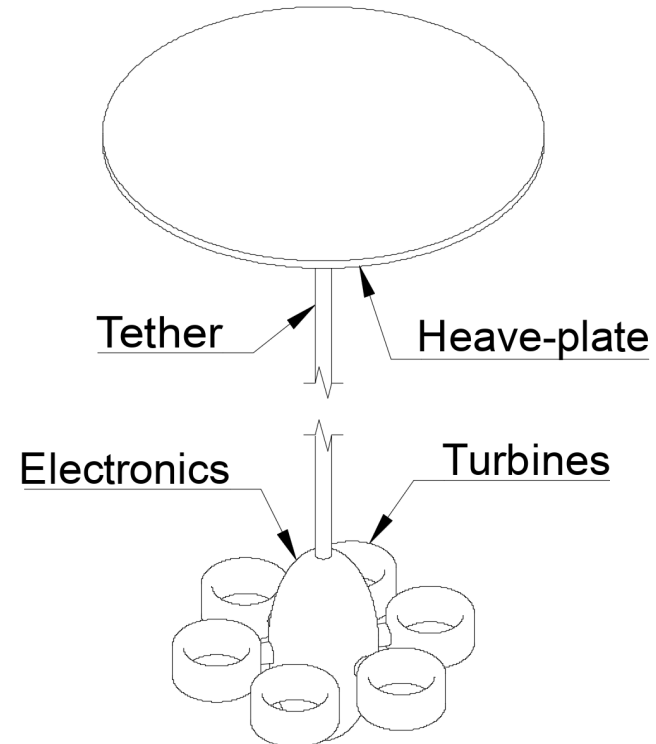


Figure 1: Conceptual drawing of a possible near-surface wave energy harvesting float.

Our proposed design (fig. 1) exploits the difference in the orbital velocities between near-surface and deep water. The device operates entirely submerged with the heave-plates in the near-surface wave field. The heave-plate transmits wave energy through the long tether into turbines attached to the ballasted electronics pod. The turbines generate power through the relative flow with the deep water where the wave field is insignificant.

Device sizing depends both on power requirements and on the expected wave environment with significant wave height  $H_s$  and energy period  $T_e$  being important factors. To avoid breaching while operating in proximity to the surface,

the device will employ active control by varying turbine PTO. Additionally, the device must be designed to avoid the tether going slack which would lower power generation and potentially cause damage. A compliant tether could assist to damp out large oscillations without slacking as well as potentially exploiting resonance.

This study explores the feasibility of the proposed design by first developing and validating a model and second exploring design parameters. Based on power consumption of common floats [13], [14], a feasible device would likely need to produce on the order of tens of watts to charge a battery capable of powering the device. A feasible design must generate sufficient power across a range of wind speeds without breaching the surface or slacking the tether.

## II. FUNDAMENTAL CONCEPTS

The design relies on wave forcing from the near-surface orbital velocity to harvest wave power. Average potential wave power  $P_w$  is defined per unit length of wave-crest length as a function (eq. 1) of significant wave height  $H_0$  and group speed  $c_g = gT_e/4\pi$ , determined by the energy period  $T_e$  for deep-water waves where  $\rho$  and  $g$  denote water density and gravitational acceleration respectively [15]. In this work we chose to use the Pierson-Moskowitz (PM) spectrum for its simplicity in light of the large parameter space to explore. For the PM spectrum both energy period and significant wave height are functions of only wind speed  $U$  [16]. Potential wave power can reach very high values even at low wind speeds. For example, 10 m/s yields 3.7 kW per meter.

$$P_w = \frac{1}{16} \rho g H_0^2 c_g \quad (1)$$

Morison's Equation (eq. 2) describes the vertical forces waves induce on bodies such as heave-plates [17]. The force  $F$  is dependent on relative flow velocity  $v_r = v_f - v$  between the body and surrounding water. The coefficients represent added mass  $C_a$  and vertical drag  $C_d$ , and the resulting force is the sum of the hydrodynamic mass and drag forces. In eq. 2,  $V$  is the volume of water contained in a sphere having a diameter equal to that of the body,  $\rho$  is the density of water, and  $A$  is the projected area of the body normal to the flow.

$$F = (\rho C_a V) \dot{v}_r + \left( \frac{1}{2} \rho C_d A \right) |v_r| v_r \quad (2)$$

The Keulegan-Carpenter (KC) number describes the relative importance of the drag forces over inertia forces for bluff objects in an oscillatory fluid flow [18]. For bodies in an oscillating flow, KC is commonly simplified (eq. 3) to only depend on wave amplitude  $a = H_0/2$  and a characteristic length  $L$ .

$$KC = \frac{2\pi a}{L} \quad (3)$$

## III. SYSTEM MODEL

We modeled the system using lumped elements analysis [19]. The heave-plates and pod both are modeled as a linear inertial element in parallel with a quadratic damping element. The tether is modeled as a linear spring. The elements are coupled together by the dynamic model (eq. 4) which is a non-linear third order system with state variables: tether force  $F_k$ , pod velocity  $v_p$ , and heave-plate velocity relative to surface velocity  $v_{sh} = v_s - v_h$ . Using the relative velocity for the heave-plates simplifies the model and sets up a control interface based on the depth from free surface.  $K$  is the tether stiffness. The subscripts  $h$  and  $p$  denoting heave-plate or pod respectively. Neither weight nor buoyancy are included in the model because the design requires cancel our for overall neutral buoyancy. Depending on the materials, this requirement could limit the mechanical design space. The model input is fluid orbital velocity  $v_f$  which is a function of time  $t$  and depth  $y_{sh}$  dependent on the wave spectrum.

$$\begin{aligned} \dot{F}_k &= K (-v_p - v_{sh} + v_f(t, y_{sh})) \\ \dot{v}_p &= \frac{1}{M_p} \left[ F_k - \left( \frac{1}{2} \rho C_p A_t \right) |v_p| v_p \right] \\ \dot{v}_{sh} &= \frac{1}{(\rho C_a V)} \left[ - \left( \frac{1}{2} \rho C_d A_h \right) |v_{sh}| v_{sh} + F_k \right] \end{aligned} \quad (4)$$

The system modeling was made simpler by several assumptions. First, we assume the tether is long enough for orbital velocity at pod depth is insignificant. Next, we ignore all parasitic drag. Finally, We assume the device has no significant effect on the motion of the surrounding water. For a real system, these assumptions either need to be incorporated into the design or will show up as inefficiencies.

Heave-plate forcing from vertical waves is described by Morrison's equation (eq. 2) where the added mass and drag coefficient are modeled from a thin disc ( $C_a = 1, C_d = 1.2$ ) or determined empirically.

In for body submerged in the wave field, the inertial frame for added mass is relative to the oscillating flow and therefore cannot be lumped directly with mass. Given a wide thin heave-plate, we assume the added mass is large enough to ignore inertial mass which reduces system complexity.

The electronics pod including the turbine housings is modeled as a point mass  $M_p$  with all inertia associated with the pod and turbines, including added mass incorporated into this single value. Due to the assumption of still water,

pod mass and added mass share an inertial frame allowing treatment as a single value for the model. In practice added mass will need to be considered in the mechanical design process.

The elastic tether is modeled as a linear spring (eq. 5) with stiffness  $K$ . Spring force depends on change in length  $F_k = K\Delta l$ . In reality the tether only provides a tension force and goes slack under compression. However, the tether will be pre-loaded by the opposing forces of the heave-plate buoyancy and ballast weight to an equilibrium. We modeled tether force as the difference from equilibrium allowing for negative tensions. This assumption holds provided the tether does not go slack ( $F_k + M_p g > 0$ ). For simplicity pod weight is set to dry weight in this analysis. Wet weight will depend on the mechanical design.

$$F_k = K\Delta l \quad (5)$$

Turbine drag is based on the PTO (eq. 6) which can be adjusted electronically by a controller. Total turbine area  $A_t$  depends on individual diameter and number of turbines. In this analysis we define turbine diameter  $D_t$  as equivalent diameter for a single turbine. Actual area and number of turbines are mechanical design choices which will affect turbine Keulegan-Carpenter (KC) number and parasitic drag. Maximum theoretical PTO is a function of the maximum power coefficient  $C_p$  which is given by the Betz limit ( $C_p = 16/27$ ) [20] or measured empirically for a specific turbine. However, turbine PTO can be manipulated electronically which changes the power coefficient.

$$P = |Fv_p| = \frac{1}{2}\rho C_p A_t |v_p|^3 \quad (6)$$

$$F = \frac{1}{2}\rho C_p A_t |v_p| v_p \quad (7)$$

By adding the variable heave-plate depth ( $\dot{y}_{sh} = v_{sh}$ ) and varying the PTO as a function of heave-plate depth, defined relative to the surface, and pod velocity it is possible to control the system's depth at the expense of reduced power generation. The system can exert control using a ratcheting effect by setting turbine power take-off, and therefore drag, high or low based on depth error, from control depth, and pod velocity to resist movement that increases error more than movement that decreases error. Electronically lowering the PTO lowers the drag preserving more overall momentum in the instantaneous direction of pod velocity. The control depth will be chosen based on maximizing power generation under an acceptable risk of surface breaching.

#### IV. PROTOTYPE TESTING

We conducted tank tests to validate our mathematical model, explore the design space related to system resonance, and show the feasibility of generating power and control

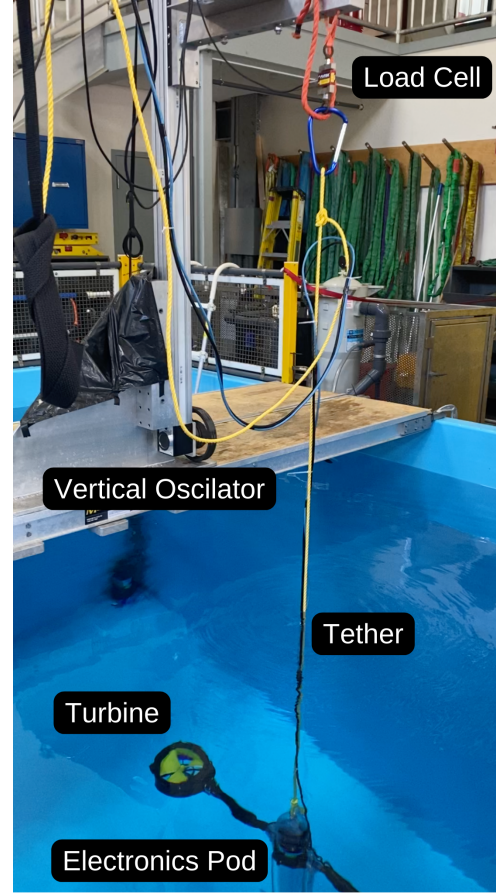


Figure 2: A prototype version of the electronics pod and two turbines is suspended in the water from a custom vertically oscillating apparatus. A force sensor provides feedback allowing the apparatus to mechanically simulate the tether force calculated from both the prototype pod movement and virtual surface heave. The apparatus tests the prototype's dynamic response and power generation from different input waves across a range of tether stiffnesses.

from the oscillating turbines on an elastic tether. For the tests a prototype pod was suspended in a vertical test tank and oscillated using a custom built testing apparatus (fig. 2) designed to simulate, through force-feedback, the effect of suspending the pod beneath the heave-plate using an elastic tether.

For the purpose for tank testing, we simplified the model to ignore heave-plate dynamics and assuming perfect coupling between the heave-plate and surface heave simplifying the model (eq. 8). Therefore, our tank tests exhibit somewhat higher power output than the same prototype would operating with a real heave-plate. Model input is the surface velocity  $v_s$  which is dependent on time  $t$  based on the wave spectrum.

$$\dot{F}_k = K(v_p - v_s(t)) \quad (8)$$

$$\dot{v}_p = \frac{1}{M_p} \left( F_k - \frac{1}{2} \rho C_p A_t |v_p| v_p \right)$$

To facilitate tank tests, we designed and fabricated an experimental apparatus (fig. 2) consisting of a Bosch 4 m vertical slide driven by a 5 hp Clearpath servo motor with the pod or various test articles suspended below in a 4 m deep tank at WHOI. Initially the device was commanded to follow a closed-loop position trajectory, either a monochromatic wave-form or a realization of the PM spectrum. These tests simulated an inextensible tether. Physical springs of sufficiently low elasticity to excite resonance proved unworkably long. To simulate the effect of an elastic tether, we instead measured vertical force on the pod and fed the result into a controller that issued torque commands to the motor.<sup>1</sup> A load cell between the sliding stage and a stiff polypropylene rope attached to the submerged device provided the measurement of vertical force on the pod.

The essential idea was to mimic the effect of a physical spring by closing the loop on force such that the measured force was driven to the theoretical (desired) force  $F_d$  created by a virtual linear spring between the virtual surface, specified as a time-varying waveform  $y_s(t)$ , and the actual pod depth  $y_p$ :

$$F_d = K(y_p - y_s). \quad (9)$$

Implementation required compensating for non-linear Coulomb friction in the apparatus and attenuating control action at frequencies above resonance to avoid exciting resonant modes in the physical system.

A prototype pod was suspended in the vertical tank from a load cell on the test apparatus arm as seen in fig. 2. The prototype consists of an aluminum frame holding a cylindrical electronics housing with two arms, each supporting a WaterLily Turbine.<sup>2</sup> The three phases of each turbine were connected to a electronic commutation circuit that included the ability to duty cycle the combined output between open-circuit and across a resistor. Power across the resistor was measured throughout testing. To alter the PTO, the duty cycle could be altered between 100% and 0%, with 100% corresponding to maximum drag and power somewhat below peak and 0% to minimum drag and zero power. Maximum PTO occurred between these extremes, however, in this work we consider a bang-bang controller switching between only maximum and minimum

<sup>1</sup>Clearpath's API does not provide access to their inner-most current/torque loop in the SC series of software controlled motors; however, with Clearpath's help, and because our system is preloaded, we were able to achieve the desired effect by continuous alteration of the torque/current limit.

<sup>2</sup><https://www.waterlilyturbine.com/>

drag. The housing included a compartment filled with lead shot to increase the weight.

For all tests, mass remained constant and the virtual surface input was a consistent monochromatic spectrum. Wave amplitude was limited by the height of the tank and amplitude gain at resonance. Using the PTO duty cycles, tests were performed with the turbines at maximum drag and minimum drag (free-wheeling). For each configuration, we tested the prototype across various virtual tether stiffnesses representing designs with natural frequencies significantly above and below the forcing frequency.

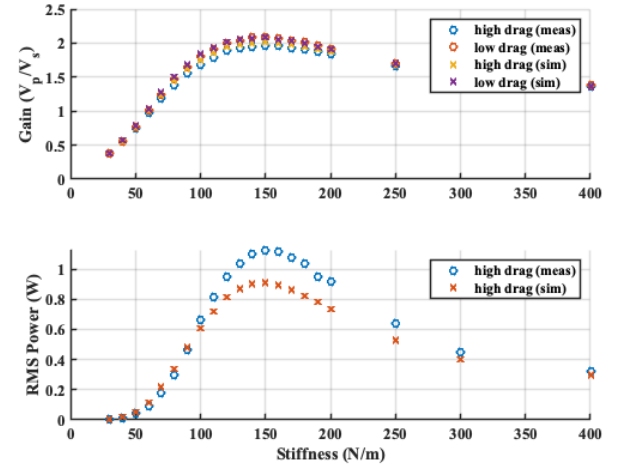


Figure 3: Summary results from tank testing of the prototype pod at various virtual tether stiffnesses: (top) the ratio of pod oscillation amplitude to virtual surface amplitude; (bottom) RMS power generated at 100% duty cycle. Resonance was observed for virtual stiffnesses near 150 N/m, with steep roll-off for more elastic springs and relatively modest roll-off for stiffer springs. Varying PTO between 0% and 100% duty cycle had a small but measurable impact on amplitude ratio. Comparison simulations use fitted drag and added mass coefficients as described in the text.

The results from the tank tests (fig. 3) show a resonant peak for both power and gain observed at a tether stiffness around 150 N/m. At lower stiffnesses, gain and power drop off quickly to zero, while at higher stiffnesses, gain and power appear to converge with gain approaching one as expected. When plotted against KC number, gain and power become linear and quadratic respectively.

For each drag configuration, we fit the complete data set to Morrison's Equation (eq. 2 to find coefficients representing mass (including added mass) and vertical drag. For the two configurations, the difference between the fitted mass was negligible. The difference in fitted drag between the two data sets is the drag contribution of the turbine PTO and therefore the drag available for both power generation and control. The remaining drag is the parasitic

drag on the system. For the prototype, parasitic drag is much greater than turbine drag, and we believe design optimizations can be made to greatly improve power output and controllability. We also fitted power coefficients for the turbines which were significantly below both the Betz limit and fitted drag coefficients. We fitted separate power and drag coefficients for positive and negative velocity because the WaterLily Turbines are not designed for bi-directional flow and have an asymmetrical shape. All of the coefficients are susceptible to over fitting due to the limited data set. To mitigate over fitting, we fitted to the entire data set rather than individual runs.

Using our fitted coefficients, we simulated each configuration using the same inputs for the tank model (eq. 8). The results (fig. 3) show the close correlation between the simulated results and the measured results. Notably, the tests showed higher gain than expected by the simulations especially at resonance. The effect is pronounced in the power curves. An example run (fig. 4) shows the measured and simulated values show close correlation throughout the test. Measured power lagged velocity in all tests. We believe this is an artifact of our testing set up.

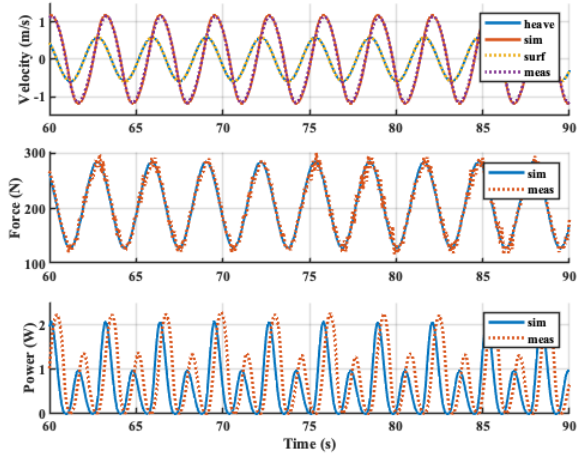


Figure 4: Results from a tank test run showing the prototype motion and power generation. The example test was conducted with power-takeoff turned high and a tether stiffness of 150 N/m, close the resonant peak of the system. The forces resulting from the fitted coefficients match the measured values from the tether load cell.

The tank tests validated the technique of fitting pod and turbine characteristics to our simplified model to predict a dynamic response and power generation. However, the tests were limited to a single prototype design under small wave amplitudes limited by the height of the tank. The tests also used the simplified model (eq. 8) which does not take into account heave-plate dynamics which will have an impact on both power conversion and control.

## V. MODEL SIMULATIONS

To evaluate a wider range of design parameters consisting of tether stiffness, pod mass, turbine area, and heave-plate diameter, we used dynamic simulations of the system mode (eq. 4). Inclusion of the heave-plate dynamics increases model complexity compared to the tank tests. However, this complexity is important to capture because the imperfect surface tracking of the heave-plate contributes to both power conversion and controllability.

We implemented a simple bang-bang controller which defaults to full power take-off except when the turbines are moving in the opposite direction as heave-plate error defined as the difference between heave-plate depth controller desired depth. For all simulations the device starts with the heave-plates at the surface and the controller is given a desired depth equal to the significant wave height of the wave spectrum.

We simulated 5000 uniformly randomly selected parameter sets using the model (eq. 4) developed earlier. Simulations used turbine PTOs based on the Betz limit and therefore overestimate power output. We used parameter values beyond reasonable limits to ensure we captured theoretical global extrema for the model. To reduce computational time and develop clearer insights, simulations were forced with a monochromatic wave form having the same significant wave height and energy period as a PM spectrum of equivalent wind speed. We also simulated selected designs using a full PM spectrum to confirm performance in a more realistic environment.

Summary results from all simulations are presented (fig. 5) in nondimensional form. The independent nondimensionalized design parameters (discussed separately below) are the frequency ratio, the heave-plate KC number, an area ratio of turbines to heave-plate, and a mass ratio between pod mass and heave-plate added mass. Several examples to be discussed are marked on the plots.

We evaluated the simulations based on power extraction efficiency  $P/P_w$  over the equivalent wave-power per heave-plate diameter and an error ratio  $\text{rms}(\text{depth error})/H_0$  of depth error to significant wave height. In all cases, power extraction efficiency values are low. Therefore system must rely on the high energy density of waves. The error ratio represents the inverse of controllability. Since the control depth for each simulation is set equal to the significant wave height, an error ratio of one represents a completely uncontrollable device. We disregarded simulations where the tether went slack at any point as invalid.

Using the non-dimensional relationships shown as point clouds (fig. 5), we are able to gain insight into the individual and combined effects of each design parameter. In particular, the upper edge of the power-gain point cloud and the lower edge of the error ratio cloud, show the best case given a set value for the corresponding parameter assuming

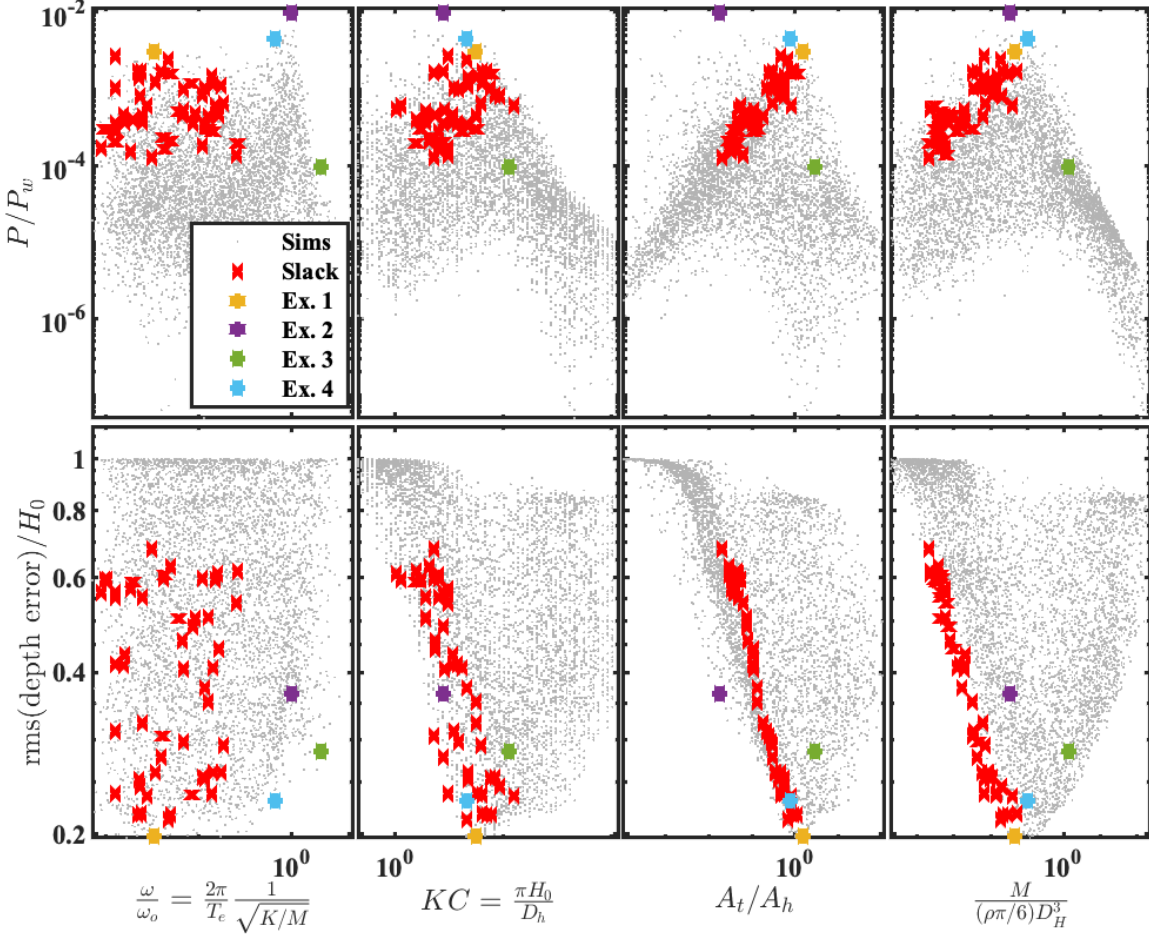


Figure 5: Non-dimensional analysis of simulation results using monochromatic spectra. The output parameters are power-gain and a depth error ratio to significant wave height. Input parameters are the ratio of the natural frequency to the wave frequency, heave-plate KC number, a turbine to heave-plate area ratio, and a ratio of pod mass to heave-plate added mass. The point clouds represent possible realizations of the parameter sets and simulation outputs. Because all simulations were started at the surface and set to a control depth equal to the significant wave height, a depth error ratio of one represents a design incapable of control. Points representing simulations which experienced tether slack events are represented by a red 'X' and can be seen concentrated in certain parameter values such as higher powered broadband devices. Ex. 1-4 represent, in order, examples of a broadband, resonant, anti-resonant, and weakly-resonant designs captured by the simulations.

all other parameters are well chosen. For example, a highly resonant with excessively large area-ratios will generate very little power or control. Alternatively a resonant design with appropriately sized turbines, but an undersized heave-plate, will be unlikely to generate power.

The ratio of a design's natural frequency of oscillation to the inverse of the wave period is given by  $(2\pi/T_e)/(\sqrt{K/M})$ . We will refer to this quantity as the frequency ratio for the sake of brevity. Power extraction efficiency shows a peak at resonance. At frequencies above resonance the power extraction efficiency falls off very quickly. Some

broadband devices are able to produce high power but slacking is common in this region. Resonance also decreases controllability due to the phase delay reducing time where the controller can exert control.

Heave-plate KC number, given by  $\pi H_0/D_h$ , is a comparison of the inertial versus drag forces on the heave-plate. Excessively high KC numbers, representing undersized heave-plates, cause power extraction efficiency to drop off quickly because small heave-plates track the surface poorly. Excessively low KC numbers, representing oversized heave-plates, track the surface too well for control to be effectively

exerted by the turbines. Lower KC numbers also experience increased risk of tether slackening. The imperfect surface tracking of smaller heave-plates may provide additional damping for large wave oscillations.

Turbine to heave-plate area-ratio, given by  $\frac{A_t}{A_h}$ , compares turbine drag to heave-plate drag. Controllability heavily depends on area ratio. Excessively high area-ratios, representing oversized turbines, fail to produce power because the high drag stifles the motion required to generate flow for power generation. Excessively low area-ratios, representing undersized turbines, also fail to generate power, and are unable to exert control over a large heave-plate. Rare exceptions exist including Ex. 2 which are likely all highly resonant designs. Effective turbine area can be reduced by electronically decreasing power-take-off.

Mass-ratio  $M/((\pi/6)\rho D_h^3)$  compares heave-plate inertia to pod inertia. Excessively high mass-ratios, representing undersized heave-plates compared to device size, produce little power or control since the large pod inertia is not significantly affected by heave-plate oscillations. Excessively low mass-ratios, representing undersized pod masses, cause the pod mass to have little effect on the dynamics of the system unless the turbines are also undersized. These designs only generate significant power and control when drag dominated as broadband devices and are susceptible to tether slackening.

In general, relatively controllable designs tend to also have relatively high power extraction efficiency. This is fortunate from the perspective of designing an actual device. Designs must balance drag and inertial effects. In the analysis, we can much more easily see infeasible designs than optimal designs since it is clear where power and control drop off and in which regions slackening occurs. Combined with the assumptions listed in the modeling and real world material limitations, we expect to reach successful design through the process of elimination.

Fig. 6 shows the simulation represented by Ex. 1 in fig. 5, which is representative of a potential broadband design. The parameter set uses a large turbine area and a stiff tether resulting in a drag dominated system. The force on the tether goes through large fluctuations approaching a slack tether. The design quickly reaches control depth and consistently sets control/PTO high represented by the square wave on the velocity plot.

However, when the same design is simulated using a PM spectrum (fig. 7) the system undergoes larger fluctuations resulting in multiple slack events and therefore does not meet design requirements. Additionally, most of the power generation comes from large spikes in both power and force which is likely unrealistic and could damage the system. When simulated at higher wind speeds, tether slackening becomes more extreme. In general, stiff broadband design require greater safety factors.

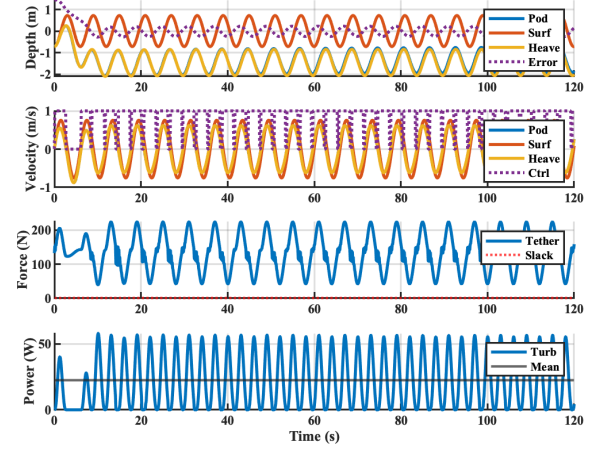


Figure 6: A simulated broadband design (Ex. 1) operating in a monochromatic waveform equivalent to 8 m/s winds. This design has a heave-plate diameter of 0.82 m, equivalent turbine diameter of 1.00 m, pod mass of 13.5 kg and tether stiffness of 13500 N/m. It generates 30 W RMS with a depth error of 0.29 m RMS.

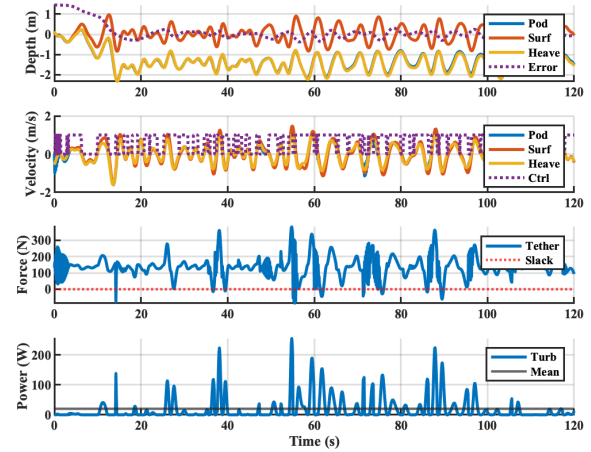


Figure 7: A simulated broadband design (Ex. 1) operating in a wave spectrum equivalent to 8 m/s winds. It generates 43 W RMS with a depth error of 0.40 m RMS. Notably, the majority of the power is generated from less common large wave fluctuations which may be unrealistic and often result in a slack tether.

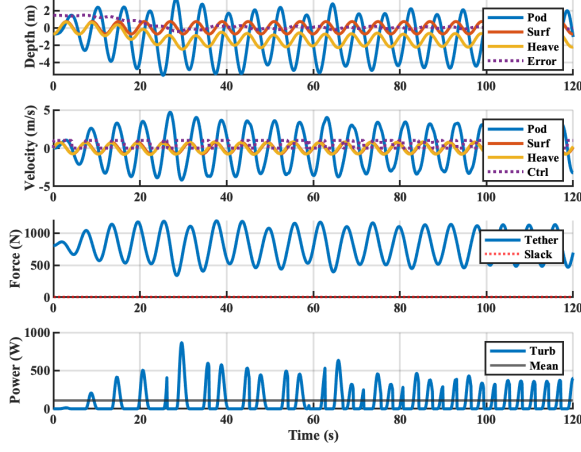


Figure 8: A simulated design (Ex. 2) operating in a monochromatic waveform equivalent to 8 m/s winds. This design has a heave-plate diameter of 1.65 m, equivalent turbine diameter of 0.22 m, pod mass of 81.9 kg and tether stiffness of 90 N/m. It generates 198 W RMS with a depth error of 0.53 m RMS.

Fig. 8 shows the simulation represented by Ex. 2 in fig. 5, which is representative of a potential resonant design. The parameter set uses a large mass with a flexible tether and a small turbine area to exploit resonance. The pod reaches high velocities generating high power despite the small turbine area. Compared to the broadband design (Ex. 1), the control reacts slower due to phase lag. Power takeoff being low often, reduces power output as well. A less aggressive controller would likely have better power output.

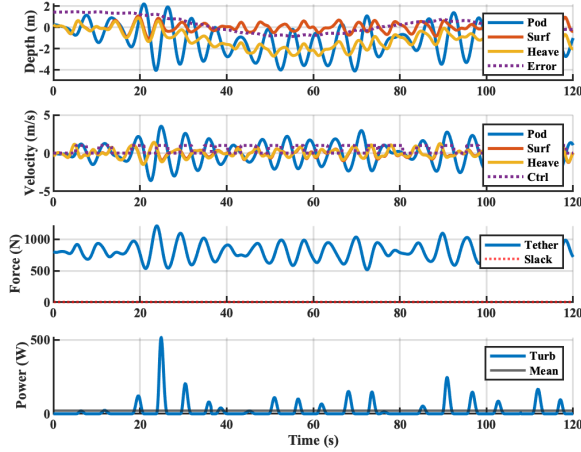


Figure 9: A simulated design (Ex. 2) operating in a wave spectrum equivalent to 8 m/s winds. It generates 61 W RMS with a depth error of 0.77 m RMS.

However, when the same design is simulated using a PM

spectrum (fig. 9), power drops as the resonance is less pronounced for a panchromatic waveform. The compliant tether effectively damps large oscillations without going slack which also smooths the power input compared to a broadband design.

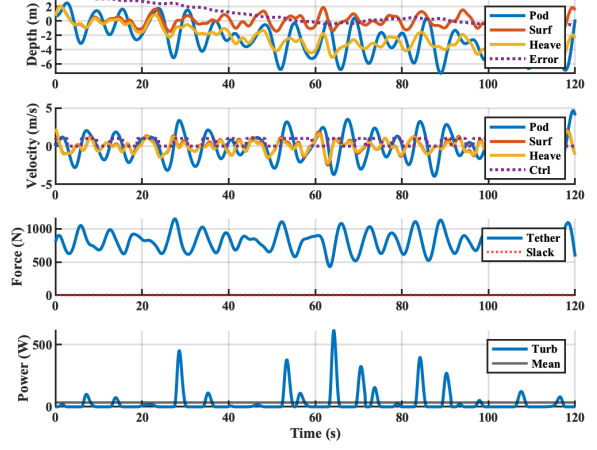


Figure 10: A simulated design (Ex. 2) operating above its peak efficiency in a wave spectrum equivalent to 12 m/s winds. It generates 95 W RMS with a depth error of 1.58 m RMS.

When simulated at a higher wind speed (fig. 10), the design does not generate significantly more power and requires more time to reach control depth. However, the compliant tether continues to effectively damp large fluctuations without slacking.

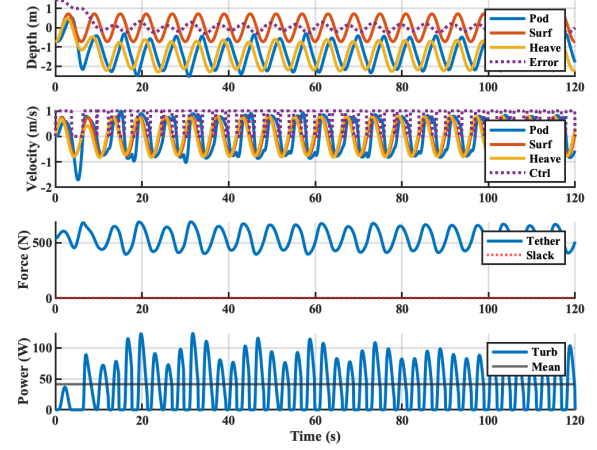


Figure 11: A simulated weakly resonant design (Ex. 4) operating in a monochromatic waveform equivalent to 8 m/s winds. This design has a heave-plate diameter of 1.00 m, equivalent turbine diameter of 0.86 m, pod mass of 54.8 kg and tether stiffness of 135 N/m. It generates 56 W RMS with a depth error of 0.33 m RMS.

Fig. 11 shows the simulation represented by Ex. 4 in fig. 5, which is representative of a weakly resonant design. The parameter set is a compromise between the broadband (Ex. 1) and resonant (Ex. 2) design which is reflected in the power extraction efficiency and depth error. When the same design simulated using a PM spectrum (fig. 12), power drops though less significantly than the resonant design. The compliant tether still effectively damps large oscillations without going slack. When simulated at a higher wind speed (fig. 10), the design does generate significantly more power and the compliant tether continues to effectively damp large fluctuations without slacking. Throughout the simulations, the weakly resonant design effectively manages depth better than the strongly resonant design.

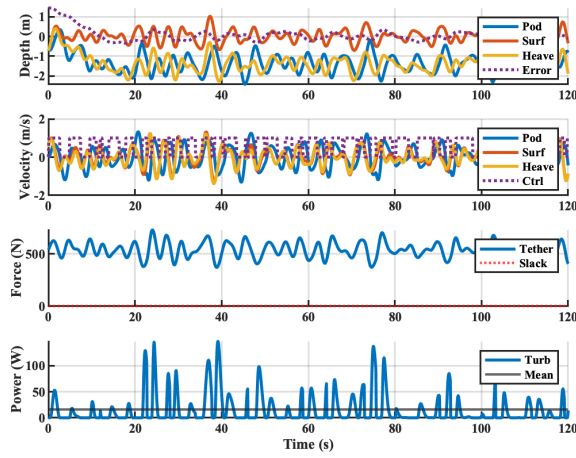


Figure 12: A simulated weakly resonant design (Ex. 4) operating in a wave spectrum equivalent to 8 m/s winds. It generates 33 W RMS with a depth error of 0.32 m RMS.

Fig. 14 shows all four examples compared across a range of wind speeds using PM spectra. All four examples have peak energy extraction efficiency at 8 m/s. However, at higher wind speeds, efficiency is less important due to the general increase in available wave power. The anti-resonant design (Ex. 3) performs worst at all wind speeds, and the broadband design (Ex. 1) experiences tether slackening even at relatively low wind speeds. The the strongly (Ex. 2) and weakly (Ex. 4) resonant designs have similar performance at higher wind speeds with slacking remaining rare. However, at lower wind speeds the weakly resonant design significantly outperforms the strongly resonant design for both power and control. For all four examples depth error increases significantly with wind speed potentially increasing the risk of a surface breach. The risk could be mitigated by setting a deeper control depth and relying on the greater depth penetration of wave power at higher wind speeds.

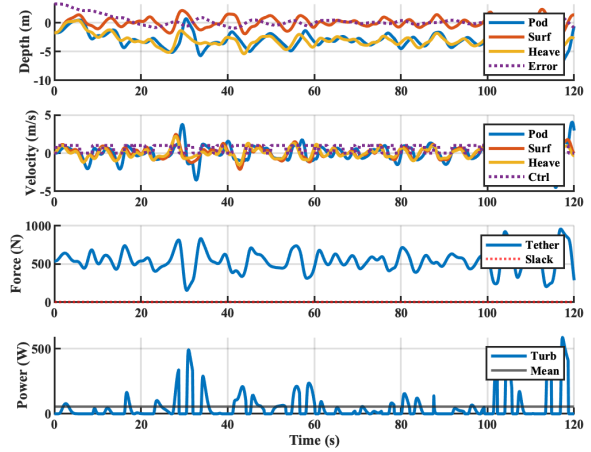


Figure 13: A simulated weakly resonant design (Ex. 4) operating above its peak efficiency in a wave spectrum equivalent to 12 m/s winds. It generates 117 W RMS with a depth error of 0.88 m RMS.

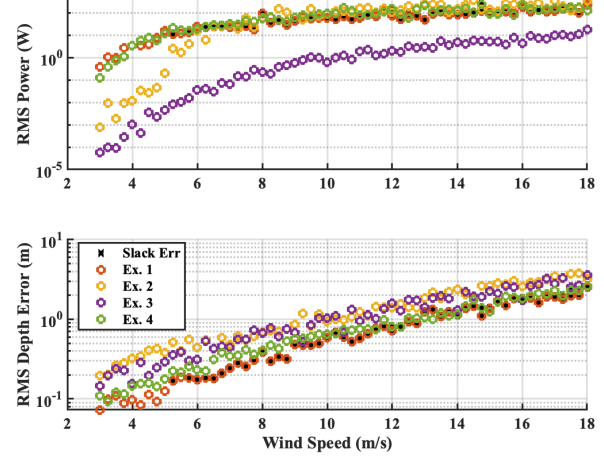


Figure 14: Example designs compared across various wind speeds. Points representing simulations which experienced tether slack events are represented by a black 'X'. Ex. 1-4 represent, in order, examples of a broadband, resonant, anti-resonant, and weakly-resonant system captured by the simulations. The weakly-resonant system (Ex. 4) performs best for both power conversion and control for the widest range of wind speeds.

## VI. CONCLUSIONS

The insights from this exploratory study show that fully untethered autonomous float could be designed that harnesses near-surface wave power for extended operations. Enough power exists in the near-surface wave field to power or recharge a small autonomous float. The wave energy could be harvested using a submerged heave plate in the oscillating wave field tethered to an energy harvesting turbine hanging below in relatively still water. Such a device could exert control through temporally lowering PTO and therefore drag. An alternative controller could use an lowered optimal PTO, and exert control by temporally increasing PTO. Using a compliant tether could allows such a device to exploit resonance for increased power extraction efficiency as well as helping to absorb large wave fluctuations. The study shows the considerations and relationships required for designing a device for a range of applications and conditions. Future work is still required to develop and deploy an ocean-going prototype.

## VII. ACKNOWLEDGEMENTS

This project was made possible by the Office of Naval Research through a grant (N00014-16-1-3037). R. Shomberg's participation in the project was funded by the Office of Naval Research NEPTUNE 2.0 Program GRANT12941723. We wish to acknowledge Andrew Billings, James Partan, Victor Naklicki, Jordan Stanway, and Jonathan Ware for their technical contributions to the project.

## REFERENCES

- [1] S. R. Jayne, D. Roemmich, N. Zilberman, S. C. Riser, K. S. Johnson, G. C. Johnson, and S. R. Piotrowicz, "The argo program: present and future," *Oceanography*, vol. 30, no. 2, pp. 18–28, 2017.
- [2] R. Rozali, M. M. Yusop, P. Khalid, W. Dahalan, A. Yahaya, N. Salih, and S. Yaakob, "Floating buoy technology for research purposes," *Int J Innov Technol Explor Eng*, vol. 8, no. 12, pp. 5514–5520, 2019.
- [3] J. Rabault, T. Nose, G. Hope, M. Müller, Ø. Breivik, J. Voermans, L. R. Hole, P. Bohlinger, T. Waseda, T. Kodaira *et al.*, "Openmetbuoy-v2021: An easy-to-build, affordable, customizable, open-source instrument for oceanographic measurements of drift and waves in sea ice and the open ocean," *Geosciences*, vol. 12, no. 3, p. 110, 2022.
- [4] D. Chu, S. Parker-Stetter, L. C. Hufnagle, R. Thomas, J. Getsiv-Clemons, S. Gauthier, and C. Stanley, "2018 unmanned surface vehicle (saildrone) acoustic survey off the west coasts of the united states and canada," in *OCEANS 2019 MTS/IEEE SEATTLE*. IEEE, 2019, pp. 1–7.
- [5] R. Xu, H. Wang, Z. Xi, W. Wang, and M. Xu, "Recent progress on wave energy marine buoys," *Journal of Marine Science and Engineering*, vol. 10, no. 5, p. 566, 2022.
- [6] C.-C. Teng, S. Cucullu, S. McArthur, C. Kohler, B. Burnett, and L. Bernard, "Buoy vandalism experienced by noaa national data buoy center," in *OCEANS 2009*. IEEE, 2009, pp. 1–8.
- [7] T. Aderinto and H. Li, "Review on power performance and efficiency of wave energy converters," *Energies*, vol. 12, no. 22, p. 4329, 2019.
- [8] A. R. Grilli, J. Merrill, S. T. Grilli, M. L. Spaulding, and J. T. Cheung, "Experimental and numerical study of spar buoy-magnet/spring oscillators used as wave energy absorbers," in *The Seventeenth International Offshore and Polar Engineering Conference*. OnePetro, 2007.
- [9] H. Xiao, Z. Liu, R. Zhang, A. Kelham, X. Xu, and X. Wang, "Study of a novel rotational speed amplified dual turbine wheel wave energy converter," *Applied Energy*, vol. 301, p. 117423, 2021.
- [10] H. Joe, H. Roh, H. Cho, and S.-C. Yu, "Development of a flap-type mooring-less wave energy harvesting system for sensor buoy," *Energy*, vol. 133, pp. 851–863, 2017.
- [11] T. Daniel, J. Manley, and N. Trenaman, "The wave glider: enabling a new approach to persistent ocean observation and research," *Ocean Dynamics*, vol. 61, no. 10, pp. 1509–1520, 2011.
- [12] R. H. Stewart, *Introduction to physical oceanography*. Robert H. Stewart, 2008.
- [13] A. E. Copping, R. E. Green, R. J. Cavagnaro, D. S. Jenne, D. Greene, J. J. Martinez, and Y. Yang, "Powering the blue economy-ocean observing use cases report," Pacific Northwest National Lab.(PNNL), Richland, WA (United States), Tech. Rep., 2020.
- [14] R. J. Cavagnaro, C. Matthews, D. Hume, R. Raye, A. Copping, and D. Jenne, "Enabling marine energy integration for ocean observing: Functional requirements," in *Global Oceans 2020: Singapore-US Gulf Coast*. IEEE, 2020, pp. 01–07.
- [15] R. Salmon, "Introduction to ocean waves," *Scripps Institution of Oceanography, University of California, San Diego*, 2008.
- [16] W. J. Pierson Jr and L. Moskowitz, "A proposed spectral form for fully developed wind seas based on the similarity theory of sa kitaigorodskii," *Journal of geophysical research*, vol. 69, no. 24, pp. 5181–5190, 1964.
- [17] A. Brown, J. Thomson, and C. Rusch, "Hydrodynamic coefficients of heave plates, with application to wave energy conversion," *IEEE Journal of Oceanic Engineering*, vol. 43, no. 4, pp. 983–996, 2017.
- [18] G. H. Keulegan, L. H. Carpenter *et al.*, "Forces on cylinders and plates in an oscillating fluid," *Journal of research of the National Bureau of Standards*, vol. 60, no. 5, pp. 423–440, 1958.
- [19] J. L. Shearer, A. T. Murphy, and H. Richardson, *Introduction to System Dynamics*, 2nd ed. Reading, Mass: Addison-Wesley, 1971.
- [20] P. Lecanu, D. Mouaze, B. Smorgrav *et al.*, "Theoretical calculation of wind (or water) turbine: Extending the betz limit," *Preprints*, 2021.